

AFRL-SN-HS-TR- 2000-010

RECONSTRUCTION ALGORITHMS FOR MWIR CHROMOTOMOGRAPHY

J.P. GARCIA
OPTICAL SCIENCES CENTER
UNIVERSITY OF ARIZONA
TUCSON ARIZONA 85721

FINAL REPORT 10 June 1999 – 10 June 2000

APPROVED FOR PUBLIC RELEASE DISTRIBUTION UNLIMITED



AIR FORCE RESEARCH LABORATORY
Sensors Directorate
80 Scott Dr
Hanscom AFB MA 01731-2909

20020716 073

TITLE OF REPORT:

Reconstruction Algorithms for MWIR Chromotomography

PUBLICATION REVIEW

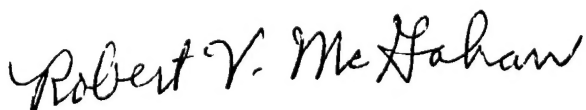
This report has been reviewed and is approved for publication.

APPROVED:



**RICHARD TAYLOR
CONTRACT MONITOR
AFRL/SNHI**

APPROVED:



**Robert V. McGahan,
Division Technical Advisor
Electromagnetics Technology Division**

REPORT DOCUMENTATION PAGE

Form Approved
OMB No. 0704-0188

Public reporting burden for this collection of information is estimated to average 1 hour per response, including the time for reviewing instructions, searching existing data sources, gathering and maintaining the data needed, and completing and reviewing the collection of information. Send comments regarding this burden estimate or any other aspect of this collection of information, including suggestions for reducing this burden, to Washington Headquarters Services, Directorate for Information Operations and Reports, 1215 Jefferson Davis Highway, Suite 1204, Arlington, VA 22202-4302, and to the Office of Management and Budget, Paperwork Reduction Project (0704-0188), Washington, DC 20503.

| | | | | |
|---|--|--|--|----------------------------------|
| 1. AGENCY USE ONLY (Leave blank) | | | 2. REPORT DATE | 3. REPORT TYPE AND DATES COVERED |
| | | | August 2000 | Final June 1999-June 2000 |
| 4. TITLE AND SUBTITLE | | | 5. FUNDING NUMBERS | |
| Reconstruction Algorithms for MWIR Chromotomography | | | F19628-99-C-0060 PE 61102F PR 2305 TASK BN WU 02 Accession # | |
| 6. AUTHOR(S) | | | 8. PERFORMING ORGANIZATION REPORT NUMBER | |
| J.P. Garcia C.E. Volin E.L. Dereniak | | | | |
| 7. PERFORMING ORGANIZATION NAME(S) AND ADDRESS(ES) | | | 9. SPONSORING/MONITORING AGENCY NAME(S) AND ADDRESS(ES) | |
| Optical Sciences Center University of Arizona Tucson, Arizona 85721 | | | Air Force Research Laboratory AFRL/SNHI Mr. Richard Taylor 80 Scott Drive Hanscom AFB MA 01731-2909 | |
| 11. SUPPLEMENTARY NOTES | | | 10. SPONSORING/MONITORING AGENCY REPORT NUMBER | |
| | | | AFRL-SN-HS-TR-2000-010 | |
| 12a. DISTRIBUTION AVAILABILITY STATEMENT | | | 12b. DISTRIBUTION CODE | |
| APPROVED FOR PUBLIC RELEASE | | | DISTRIBUTION UNLIMITED Statement "A" | |
| | | | ESC-00-1409 | |
| 13. ABSTRACT (Maximum 200 words) | | | | |
| Two methods of chromatographic reconstruction applicable to the MWIR region of the electromagnetic spectrum were investigated. The first method involved the decomposition of the datacube into principal component space using the center order, broadband image to form and estimate the spatial components. Then this estimate was used to deconvolve an estimate of the spectral components. The second method used an extension of the traditional maximum-likelihood approach to suppress signal-independent noise in reconstructions of simulated low background scenes. | | | | |
| 14. SUBJECT TERMS | | | 15. NUMBER OF PAGES | |
| Chromatography, MWIR, image reconstruction | | | 32 | |
| | | | 16. PRICE CODE | |
| 17. SECURITY CLASSIFICATION OF REPORT | | 18. SECURITY CLASSIFICATION OF THIS PAGE | 19. SECURITY CLASSIFICATION OF ABSTRACT | 20. LIMITATION OF ABSTRACT |
| Unclassified | | Unclassified | Unclassified | UL |

TABLE OF CONTENTS

| | | |
|------|---|----|
| I. | INTRODUCTION..... | 1 |
| II. | PRINCIPAL COMPONENTS METHOD..... | 2 |
| III. | EXTENDED MAXIMUM LIKELIHOOD METHOD..... | 9 |
| IV. | CONCLUSION..... | 26 |
| V. | REFERENCES..... | 27 |

SUMMARY

Two different methods of chromatographic reconstruction applicable to the MWIR were investigated by the Optical Sciences Center, University of Arizona for The Air Force Research Laboratory (AFRI/SNHI) at Hanscom Air Force Base, Hanscom, MA. The first method involved the decomposition of the datacube into principal component space, using the center order broadband image to estimate the spatial principal components, then using this estimate to deconvolve an estimate of the spectral principal components. The second method used an extension of the traditional maximum-likelihood approach to suppress noise in reconstructions of simulated low background scenes.

PREFACE

This final report describes development of reconstruction algorithms for MWIR chromatotomography by the University of Arizona's Optical Sciences Center for The Air Force Research Laboratory (AFRI/SNHI) at Hanscom Air Force Base, Hanscom, MA. The principal investigator was E. L. Dereniak.

The authors wish to thank Tom Hamilton of SMDTC, Huntsville, AL for providing the 512 x 512 InSb snapshot camera used to collect data for this project.

I. INTRODUCTION

Chromotomographic imaging spectrometers have been operating successfully in the visible region of the electromagnetic spectrum for several years. Recently, however, there has been heightened interest in adapting the technology to wavelengths beyond one micron. In addition to the group at Hanscom AFB, the Optical Detection Lab at the Optical Sciences Center, University of Arizona has developed a prototype MWIR computed tomography imaging spectrometer (CTIS). The prototype system utilizes a simple binary phase disperser fabricated in GaAs and a 512x512 InSb snapshot camera.

Standard reconstruction techniques such as Expectation-Maximization¹ and MART² have been used with some success to reconstruct object cubes from the raw snapshots produced by this instrument. This report documents investigations of two new reconstruction techniques. The first method, designated here as "Principal Component Method", shows potential for increased reconstruction speed. The second method, designated here as "Extended Maximum Likelihood Method", demonstrates increased immunity to signal-independent noise in the raw data.

II. PRINCIPAL COMPONENT METHOD

The forward action of tomographic imaging spectrometers is described either by theoretical model³ or by experimental measurement⁴. The goal of our software development is to invert the problem to form an estimate of the object cube from the raw data collected by the spectrometer. Traditional techniques such as pseudoinverse and iterative algorithms have been applied to yield acceptable reconstructions. More advanced algorithms are required to improve results using *a priori* information about target scenes and the imaging system.

Experiments performed at the University of Arizona apply to the second-generation MWIR Computed Tomography Imaging Spectrometer (CTIS). The instrument employs a simple, binary phase Computer Generated Hologram (CGH) to produce several simultaneous tomographic projections of the 3D object cube onto a large-format Focal plane array. The result is a non-scanning, flash imaging spectrometer. The current MWIR CTIS operates in the 3.0-5.0 μm band. The current CGH limits the system to five useful projections onto a 512×512 focal plane array. The spectral accuracy of the instrument is limited to about 21 bands by the low number of projections.

Recent work has investigated the decomposition of the datacube into principal-component space,

$$f(x, y, \lambda) = \sum_{n=1}^R u_n(x, y) \cdot v_n(\lambda) \cdot w_n \quad (1)$$

The set of orthonormal vectors $\{v_n\}$ represents the spectral principal components of the datacube and is complete in the spectral space. The set of orthonormal images $\{u_n\}$ are the principal component images corresponding to $\{v_n\}$. The values of w indicate the contribution of the n^{th} principal component to the composite datacube. R represents the number of non-zero values of w , which for a discretized datacube may be less than or equal to the number of wavelength samples.

Any order in the CTIS raw image can be expressed analytically using the datacube decomposition from (1). Equation (2) expresses the raw image orders as a convolution of the principal component image and principal component spectrum.

$$g_j(x, y) = \sum_{n=1}^R w_n \cdot u_n(x, y) * * [v'_n(m_j \bar{r} \cdot \hat{r}_j) \cdot t'_j(m_j \bar{r} \cdot \hat{r}_j) \delta(\bar{r} \cdot \hat{r}_{\perp j})] \quad (2)$$

The order index is j , \hat{r}_j is the unit vector expressing the diffraction angle of the order, and m is a scaling factor proportional to the order's diffraction angle. $v'_n(m_j \bar{r} \cdot \hat{r}_j)$ is a two-dimensional representation of the spectral principal component; $v'_n(m_j \bar{r} \cdot \hat{r}_j) = v_n(\lambda)$. Similarly, $t'_j[m_j \bar{r} \cdot \hat{r}_j]$ is the 2D representation of the CTIS transmission, responsivity, and order diffraction efficiency as a function of wavelength, $t(\lambda)$. This equation is derived by expanding the 3D tomography expression into the principal components basis set.

The potential of this expression for the raw image is revealed by Fourier transforming (2) with $R=1$, $\bar{\rho} = \xi \hat{\xi} + \eta \hat{\eta}$:

$$G_j(\xi, \eta) = w_0 \cdot U_0(\xi, \eta) \cdot [V'_0(\bar{\rho} \cdot \hat{r}_j) * * T'_j(\bar{\rho} \cdot \hat{r}_j)] \quad (3)$$

This expression was simplified by setting the m_j term to 1, which is reasonable for a discretized system in which the sampling of the spectrum corresponds to exactly one pixel of dispersion in the first order. The Fourier transform of an order is the *product* of the Fourier transform of the spatial principal component and the 2D representation of the Fourier transform of the spectral principal component.

To form an estimate of the datacube using this technique, it is necessary to impose a constraint that the datacube is dominated by the first principal component ($w_1 > 10w_2$). Several non-overlapping orders must also exist in the raw image. The initial estimate for u_0 is the center order from the raw image. Dividing G_j by U_0 yields an estimate of the principle component spectrum. Terms \hat{r}_j and T'_j are known from calibration data, as well as small corrections in the diffraction angle due to tilt of the CGH.

Figure 1 shows the extracted order images from an MWIR CTIS raw image of a warm coffee cup. Figure 2 shows the Fourier transforms of the center and diffraction images of the same image. Multiple orders contribute more estimates of v_0 , however, some orders will have better estimates of some parts of the spectrum than others (for instance, notice the structure oriented at about 145° in the center order of Figure 2 is

represented strongly in the lower left and upper right diffraction image spectra, where the diffraction angle is nearly orthogonal to the structure). Thus, a regularized ratio may be used to reduce noise and weight the contributions to the spectra. This technique assumes that $t_j(\lambda)$ is constant for all orders used, but that is a reasonable assumption for a properly designed CGH.

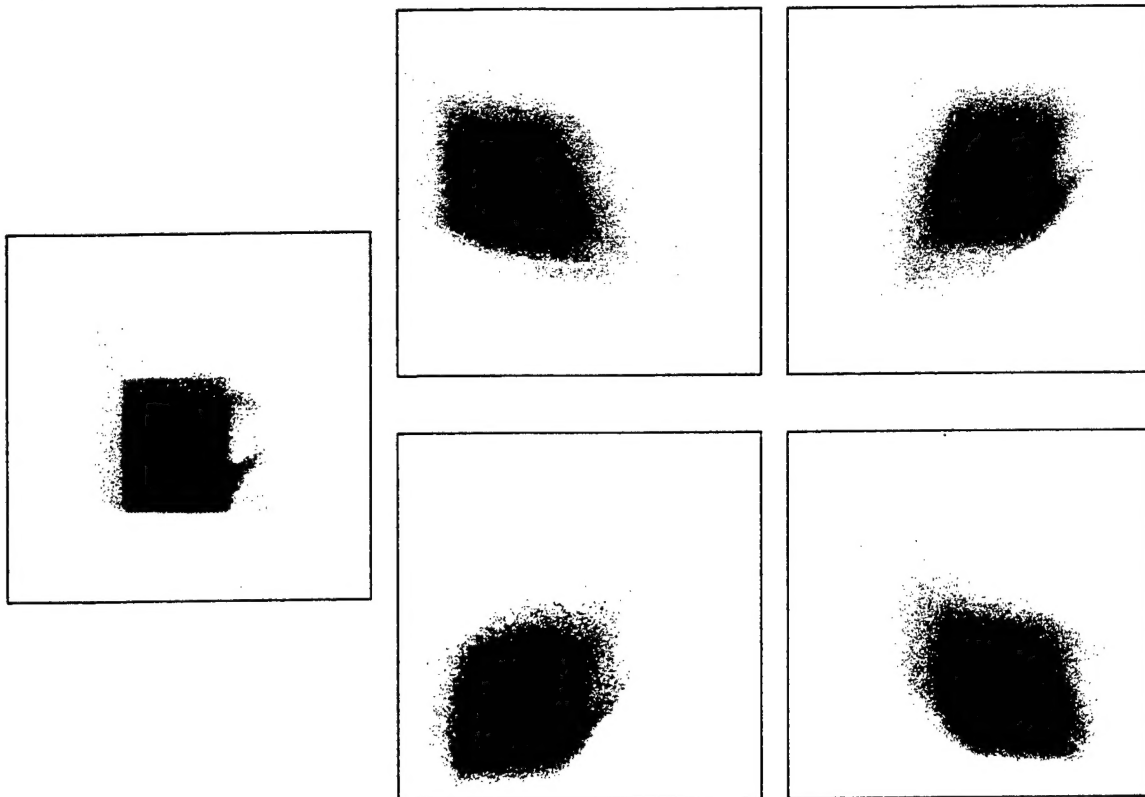


Figure 1. Order images extracted from an MWIR CTIS raw image of a warm coffee cup. The image at left is the center order. The arrangement of the diffraction images corresponds to their alignment on the FPA. The image satisfies the requirement of a dominant first principal component since the scene has nearly uniform emissivity and temperature.

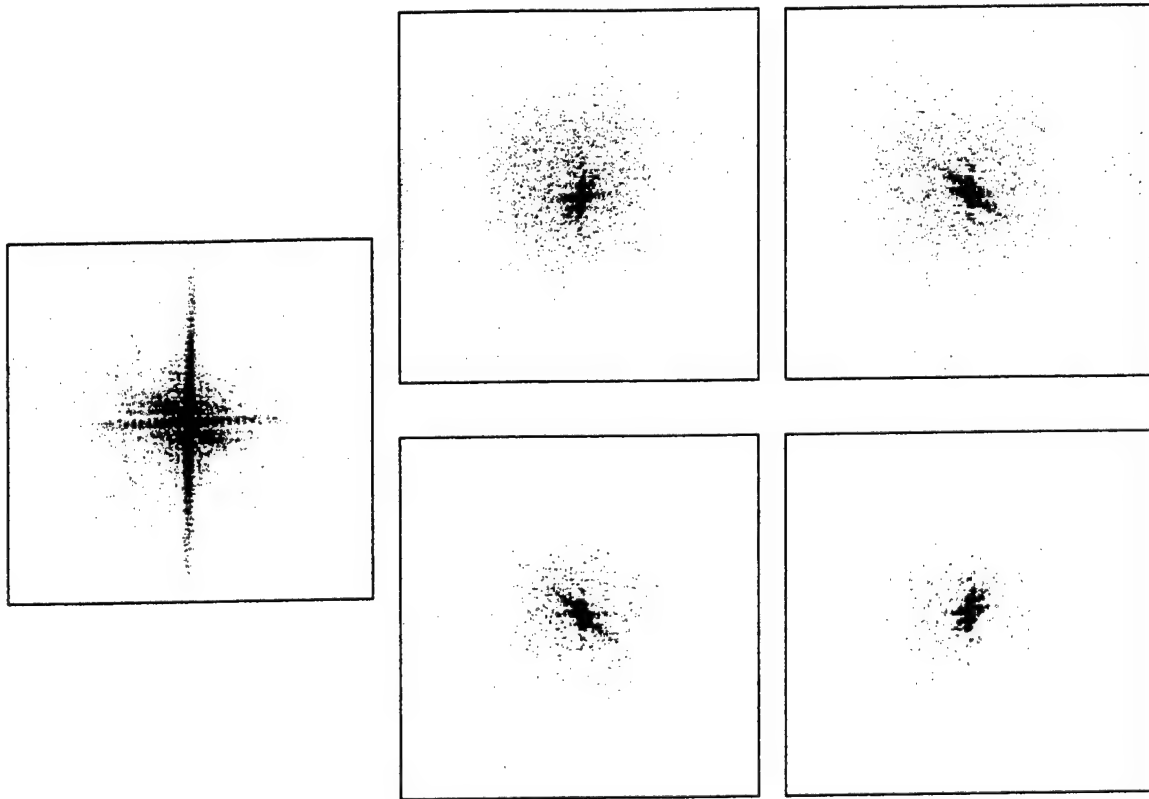
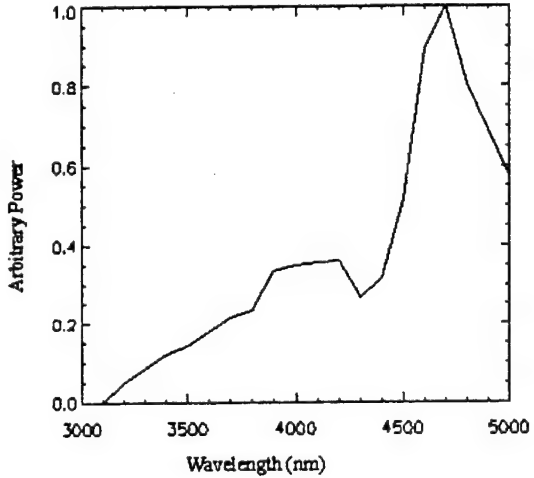


Figure 2. FFTs of order images extracted from an MWIR CTIS raw image (displayed using a logarithmic scaling of the FFT amplitude). The arrangement is identical to their respective images in Figure 1.

There are two constraints which may be imposed to improve the spectrum estimate. The first principal component spectrum must be positive and it must be zero outside of the transmission band of the spectrometer. Since these constraints are both imposed on the real spectrum, an iterative retrieval algorithm may be used to recover data at frequencies not present in the object. The results of an example recovery using only the positivity constraint are demonstrated for the coffee cup image in Figure 3.

Figure 3. Results of an iterative retrieval of the first principal component from an MWIR image of a coffee cup.



Equation 3 may be used to estimate the first principle component image, u_0 , from the diffracted orders and the estimate of v_0 . In this case, dividing G_j by V_0 yields an estimate of the principle component image. The estimation of the full (ξ, η) plane is far from complete for the second generation MWIR CTIS since the raw image has only four orders (and only two independent \hat{r} directions).

As with the principal component spectrum estimate, constraints in the image space allow an iterative recovery of parts of the missing spatial frequency data. The constraints are similar to those of the spectrum since the boundaries of the field stop are known and the first component must be non-negative (subject to the non-negativity constraint of the image). In addition, it is possible to impose the constraint that the component images must be zero wherever the center order is zero. This approach would only be unreasonable if the diffraction order efficiency into the center order were very low for any wavelength range, which is not true of any of the CGH gratings currently in use.

The results of a spatial component estimate are shown in Figure 4. Part (a) clearly shows a recovery of the horizontal and vertical structures (corresponding to crossed sinc functions present in the FFT of a square cup and a square field stop). The diagonal structures are an artifact of the limited number of projections and are clearly evident in the corresponding image (Figure 4b).

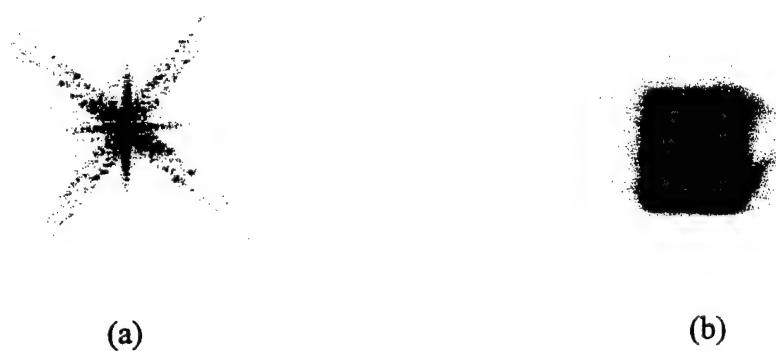


Figure 4. Advanced initial estimate of u_0 for the coffee cup image (Figure 1). (a). Center image and positivity constraints applied to $U_0(\xi, \eta)$ (logarithmic scaling). (b) FFT of $U_0(\xi, \eta)$ after 15 iterations of the constraint algorithm.

Reassembling the initial estimates of $u_0(x, y)$ and $v_0(\lambda)$ into a CTIS raw image estimate ($\hat{g}(x, y)$) according to (2) recovers for 83% of the image data (root-square sum). About 5% of the image data residual can be attributed to noise. Since the raw image does not contain the complete object cube information, the estimated datacube would have a lower accuracy compared to the object cube.

Subtracting the estimate from the raw image leaves a new raw image without the first principal component. An attempt to recover the second component is possible, but most of the constraints which applied to the first principal component are no longer valid. The center order is not a reasonable estimate of the second principal component image and the positivity constraint for either the spectrum or the image do not apply. Only the constraints on image and spectrum boundaries may be employed.

Based on experiments using several images, the second estimate typically recovers an additional 8% of the raw image information. Instead of estimating the second component, the first component may be used to form a datacube which is used as

an initial estimate for an iterative reconstruction. With more orders or a raw image with less noise, the contribution of the second component may become useful.

III. EXTENDED MAXIMUM LIKELIHOOD METHOD

Of particular interest to our group at the Optical Detection Lab are tomographic reconstruction algorithms suitable for MWIR low background applications due to our recent involvement with BMDO and due to recent interest from members of the astronomy community. The problem of detecting a thermally dim object against a dark background, which may be dominated by camera system noise rather than photon noise, is one that requires a modification of our conventional approaches. Heretofore we have assumed that either signal dependent or signal independent noise alone characterized the entire image.

Recently, a step toward the solution of the mixed noise problem was undertaken by Garcia and Dereniak⁵. The MERT algorithm achieved some success in reconstructing images in which the background was dominated by system noise and the "bright" portions of the image were relatively dim. However, system noise suppression was not entirely satisfactory. Furthermore, a literature search revealed that algorithms proven to deal effectively with this situation were generally too slow for our purposes. This section details the derivation and initial testing of a new algorithm designed to remedy these problems.

Derivation

The derivation begins identically to MERT⁵, but with one critical difference. The signal dependent photon noise is treated as a normal point process rather than a normal continuous process. This approach is an inherently more accurate description of photon statistics arising from the quantum nature of light. As before,

$$\mathbf{g} = \mathbf{Hf} + \mathbf{n1} + \mathbf{n2} \quad (5)$$

The elements of the measurement vector \mathbf{g} represent the number of detected photons per pixel during one integration time in our imaging system; the elements of the object vector

\mathbf{f} represent the number of photons emitted during one integration time for each resolution element of the object. The matrix \mathbf{H} is essentially a discrete representation of the imaging system's point spread function. Both vectors are convenient ways of expressing a two-dimensional array in a one-dimensional format to ensure that \mathbf{H} can be expressed as a two-dimensional matrix rather than a rank four, or higher, tensor. The matrix element H_{ij} gives the contribution of object element f_j to measurement element g_i . We wish to find the most likely noiseless object \mathbf{f} that could have produced the measurement \mathbf{g} in the presence of photon noise, represented by $\mathbf{n1}$, and post-detection noise, represented by $\mathbf{n2}$.

To apply the Maximum Likelihood principle, we will assume that the signal-independent system noise, $\mathbf{n2}$, is a Normal continuous distribution with zero mean and standard deviation σ_s , which can be measured. We will further assume that each Poisson distributed $(\mathbf{Hf})_m + \mathbf{n1}_m$ is well approximated by a signal-dependent Normal point distribution with mean $(\mathbf{Hf})_m$ and variance $(\mathbf{Hf})_m$. This holds true when $(\mathbf{Hf})_m$ is greater than or equal to ten⁶. With these assumptions, g_m is the sum of two statistically independent normal random variables, one continuous with a zero mean and variance σ_s and the other discrete with mean and variance equal to $(\mathbf{Hf})_m$. The probability density of measuring g_m photons in the presence of photon noise at the m^{th} detector given some object emission distribution \mathbf{f} is

$$p_1(g_m | \mathbf{f}) = \sum_{i=0}^{\infty} \frac{1}{\sqrt{2\pi(\mathbf{Hf})_m}} \exp\left\{-\frac{[g_m - (\mathbf{Hf})_m]^2}{2(\mathbf{Hf})_m}\right\} \delta(g_m - i) \quad (6)$$

The summation of weighted delta functions in this expression reflects the fact that the photon noise is quantized. The probability density of measuring g_m photons in the presence of the system noise floor is

$$p_2(g_m | \sigma_s) = \frac{1}{\sqrt{2\pi\sigma_s^2}} \exp\left\{-\frac{g_m^2}{2\sigma_s^2}\right\} \quad (7)$$

The probability density in the presence of both noise sources is the convolution of the two densities.

$$p_T(g_m | \mathbf{f}, \sigma_s) = p_1(g_m | \mathbf{f}) * p_2(g_m | \sigma_s) \quad (8)$$

or explicitly,

$$p_T(g_m | \mathbf{f}, \sigma_s) = \frac{1}{2\pi\sigma_s} \sum_{i=0}^{\infty} \exp\left\{-\frac{[g_m - (\mathbf{H}\mathbf{f})_m]^2}{2(\mathbf{H}\mathbf{f})_m}\right\} \exp\left\{-\frac{[g_m - i]^2}{2\sigma_s^2}\right\} \delta(g_m - i) dg_m \quad (9)$$

Carrying out the integration and considering all detector positions as statistically independent gives the probability of seeing some image \mathbf{g} for an object \mathbf{f} .

$$p_T(\mathbf{g} | \mathbf{f}, \sigma_s) = \frac{1}{2\pi\sigma_s} \prod_{m=1}^M \sum_{i=0}^{\infty} \exp\left\{-\frac{[i - (\mathbf{H}\mathbf{f})_m]^2}{2(\mathbf{H}\mathbf{f})_m}\right\} \exp\left\{-\frac{[g_m - i]^2}{2\sigma_s^2}\right\} \quad (10)$$

Taking the natural log in the hope of producing a more tractable function of the object estimate $\hat{\mathbf{f}}$ yields

$$\ln[p_T(\mathbf{g} | \hat{\mathbf{f}}, \sigma_s)] = -\ln(2\pi\sigma_s) + \sum_{m=1}^M \ln \left[\sum_{i=0}^{\infty} \exp\left\{-\frac{[i - (\mathbf{H}\hat{\mathbf{f}})_m]^2}{2(\mathbf{H}\hat{\mathbf{f}})_m}\right\} \exp\left\{-\frac{[g_m - i]^2}{2\sigma_s^2}\right\} \right] \quad (11)$$

To find a maximum likelihood estimate of the object, we take the partial derivative with respect to a test estimate of the number of photons emitted from the n^{th} element and insist that it equal zero.

$$\frac{\partial}{\partial \hat{f}_n} \ln[p_T(\mathbf{g} | \hat{\mathbf{f}}, \sigma_s)] = 0 \quad (12)$$

Using the fact that

$$\frac{\partial(\mathbf{H}\hat{\mathbf{f}})_m}{\partial\hat{f}_n} = \frac{\partial(\sum_i H_{mi}\hat{f}_i)}{\partial\hat{f}_n} = H_{mn} \quad (13)$$

we arrive at an equality which maximizes the likelihood.

$$\sum_{m=1}^M \left\{ \frac{\sum_{i=0}^{\infty} \left[\frac{i}{(\mathbf{H}\hat{\mathbf{f}})_m} \right]^2 \exp \left\{ -\frac{[i - (\mathbf{H}\hat{\mathbf{f}})_m]^2}{2(\mathbf{H}\hat{\mathbf{f}})_m} \right\} \exp \left\{ -\frac{[g_m - i]^2}{2\sigma_s^2} \right\} H_{mn}}{\sum_{i=0}^{\infty} \exp \left\{ -\frac{[i - (\mathbf{H}\hat{\mathbf{f}})_m]^2}{2(\mathbf{H}\hat{\mathbf{f}})_m} \right\} \exp \left\{ -\frac{[g_m - i]^2}{2\sigma_s^2} \right\}} \right\} = \sum_{m=1}^M \{H_{mn}\} \quad (14)$$

We can formulate an iterative algorithm for the best current estimate of each element of \mathbf{f} by using (10) above in a correction factor which is applied to the previous estimate of each element of \mathbf{f} .

$$\hat{f}_n^{k+1} = \hat{f}_n^k \frac{\sum_{m=1}^M \frac{H_{mn}}{(\mathbf{H}\hat{\mathbf{f}}^k)_m} \left[\frac{\sum_{i=0}^{\infty} i^2 \exp \left\{ -\frac{[i - (\mathbf{H}\hat{\mathbf{f}}^k)_m]^2}{2(\mathbf{H}\hat{\mathbf{f}}^k)_m} \right\} \exp \left\{ -\frac{[g_m - i]^2}{2\sigma_s^2} \right\}}{\sum_{i=0}^{\infty} \exp \left\{ -\frac{[i - (\mathbf{H}\hat{\mathbf{f}}^k)_m]^2}{2(\mathbf{H}\hat{\mathbf{f}}^k)_m} \right\} \exp \left\{ -\frac{[g_m - i]^2}{2\sigma_s^2} \right\}} \right]}{\sum_{m=1}^M H_{mn}} \quad (15)$$

Implementation of this algorithm, as written, is extremely computationally intensive, making it too slow for our purposes. Even though the summations over i can be truncated to plus or minus $5\sigma_s$ about g_m , if $\sigma_s = 10$ then conceivably as many as $M \times 200$ terms must be computed for each element of \mathbf{f} where M is the number of elements of \mathbf{g} . Surely there must be a faster way.

Fortunately the sums over i appear as a ratio, raising the possibility of approximating the numerator and denominator by the area under the continuous curve defined by the product of normal functions rather than explicitly adding up the value of

this product at many discrete points. If these areas can be expressed in closed form, then significant computational savings will result. The concept is illustrated in Figure 5.

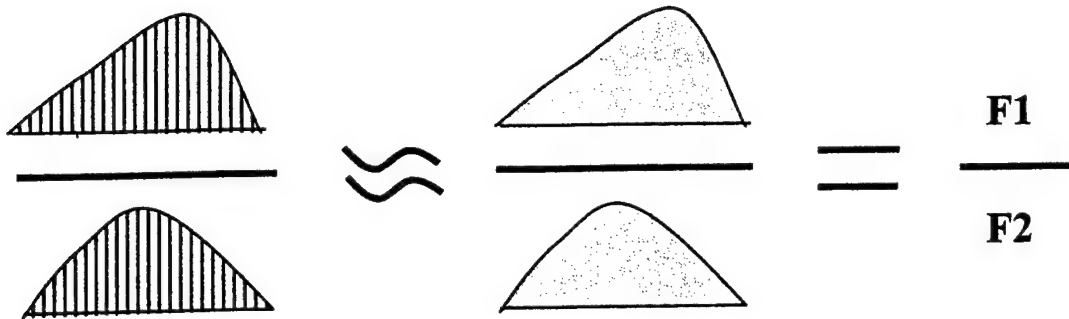


Figure 5. A ratio of two envelopes evaluated at many discrete points can be approximated by the ratio of the areas under the envelopes which hopefully can be expressed in closed form. The approximation should be good when the spacing of the discrete evaluation points is small enough that the envelope doesn't change appreciably in between points.

The approximations involved can be expressed by the following relations.

$$\sum_{i=0}^{\infty} i^2 \exp \left\{ -\frac{\left[i - (\hat{Hf}^k)_m \right]^2}{2(\hat{Hf}^k)_m} \right\} \exp \left\{ -\frac{[g_m - i]^2}{2\sigma_s^2} \right\} \Rightarrow \sum_{i=0}^{20(\hat{Hf}^k)_m} i^2 \exp \left\{ -\frac{\left[i - (\hat{Hf}^k)_m \right]^2}{2(\hat{Hf}^k)_m} \right\} \exp \left\{ -\frac{[g_m - i]^2}{2\sigma_s^2} \right\} di \quad (16)$$

$$\sum_{i=0}^{\infty} \exp \left\{ -\frac{\left[i - (\hat{Hf}^k)_m \right]^2}{2(\hat{Hf}^k)_m} \right\} \exp \left\{ -\frac{[g_m - i]^2}{2\sigma_s^2} \right\} \Rightarrow \sum_{i=0}^{20(HF^k)_m} \exp \left\{ -\frac{\left[i - (\hat{Hf}^k)_m \right]^2}{2(\hat{Hf}^k)_m} \right\} \exp \left\{ -\frac{[g_m - i]^2}{2\sigma_s^2} \right\} di \quad (17)$$

and the reduction to closed-form can be written

$$\int_0^{20(\hat{Hf}^k)_m} i^2 \exp\left\{-\frac{[i - (\hat{Hf}^k)_m]^2}{2(\hat{Hf}^k)_m}\right\} \exp\left\{-\frac{[g_m - i]^2}{2\sigma_s^2}\right\} di = F1[(\hat{Hf}^k)_m, g_m, \sigma_s^2] \quad (18)$$

$$\int_0^{20(\hat{Hf}^k)_m} \exp\left\{-\frac{[i - (\hat{Hf}^k)_m]^2}{2(\hat{Hf}^k)_m}\right\} \exp\left\{-\frac{[g_m - i]^2}{2\sigma_s^2}\right\} di = F2[(\hat{Hf}^k)_m, g_m, \sigma_s^2] \quad (19)$$

The integrals have been carried out to 19 standard deviations past the mean, $(\hat{Hf})_m$, of the first exponential term in the integrands to approximate an infinite upper limit. Little computational penalty is incurred by such mathematical overkill by inspection of the explicit forms of F1 and F2. The expressions themselves do not become more complex as the upper limit increases provided it remains finite. Only coefficients in the expressions change.

$$F1(a, b, c) = -\frac{1}{2} a^{3/2} \sqrt{c} \exp\left[-\frac{b^2 + ac}{2c}\right] \left\{ -\frac{2\sqrt{a}\sqrt{c}(b+c)}{(a+c)^2} - \frac{(c^2 + a(b^2 + c + 2bc + c^2)) \exp\left[\frac{a(b+c)^2}{2c(a+c)}\right] \sqrt{2\pi} \operatorname{Erf}\left[\frac{\sqrt{a}(b+c)}{\sqrt{2\sqrt{c}\sqrt{a+c}}}\right]}{(a+c)^{5/2}} \right\} \\ + \\ \frac{1}{2} a^{3/2} \sqrt{c} \exp\left[-\frac{b^2 + ac}{2c}\right] \left\{ \frac{2\sqrt{a}\sqrt{c}(20a + b + 21c) \exp\left[-\frac{20a(10a - b + 9c)}{c}\right]}{(a+c)^2} + \frac{(c^2 + a(b^2 + c + 2bc + c^2)) \exp\left[\frac{a(b+c)^2}{2c(a+c)}\right] \sqrt{2\pi} \operatorname{Erf}\left[\frac{\sqrt{a}(20a - b + 19c)}{\sqrt{2\sqrt{c}\sqrt{a+c}}}\right]}{(a+c)^{5/2}} \right\} \quad (20)$$

$$F2(a, b, c) = \frac{\sqrt{a}\sqrt{c}\exp\left[-\frac{(a-b)^2}{2(a+c)}\right]\sqrt{\frac{\pi}{2}}\text{Erf}\left[\frac{\sqrt{a}(b+c)}{\sqrt{2}\sqrt{c}\sqrt{a+c}}\right]}{\sqrt{a+c}} + \frac{\sqrt{a}\sqrt{c}\exp\left[-\frac{(a-b)^2}{2(a+c)}\right]\sqrt{\frac{\pi}{2}}\text{Erf}\left[\frac{\sqrt{a}(20a-b-19c)}{\sqrt{2}\sqrt{c}\sqrt{a+c}}\right]}{\sqrt{a+c}} \quad (21)$$

With $a = (\mathbf{H}\hat{\mathbf{f}}^k)_m$, $b = g_m$, $c = \sigma_s^2$, the algorithm can be written concisely as

$$\hat{f}_n^{k+1} = \hat{f}_n^k \frac{\sum_{m=1}^M \frac{H_{mn}}{(\mathbf{H}\hat{\mathbf{f}}^k)_m^2} \left[\frac{F1((\mathbf{H}\hat{\mathbf{f}}^k)_m, g_m, \sigma_s^2)}{F2((\mathbf{H}\hat{\mathbf{f}}^k)_m, g_m, \sigma_s^2)} \right]}{\sum_{m=1}^M H_{mn}} \quad (22)$$

Since the error function can be easily implemented in a look-up table, F1 and F2 can be considered general closed-form approximations to the nasty summations over i in (15).

Discussion

We wish to note in passing the similarity between this algorithm and algorithms developed by Snyder⁷ and Llacer and Nunez⁸ to deconvolve the initially blurred Hubble Space Telescope images. Their techniques modeled the photon noise as a Poisson point process and the system noise as a Gaussian continuous process. They arrived at an expression of similar computational complexity to (15) but were unable to find *general* closed-form approximations. Consequently these methods produced superb results, but ran with agonizing slowness except for certain *special* cases when approximations could be made. This is not a problem if an overnight run to reconstruct a single image is tolerable. Initial comparisons of runtimes indicate that our new technique is roughly 30 times faster.

Initial tests of the new algorithm against its predecessor, MERT, were conducted to gauge relative performance on a simple reconstruction problem. An optical system with an x-y separable Gaussian PSF and system noise equal to signal photon noise was

simulated with a Monte Carlo program that computes individual photon trajectories to accurately simulate quantum spatial noise. The original 17 x 17 pixel object and noisy blurred 17 x 17 pixel image are shown below.

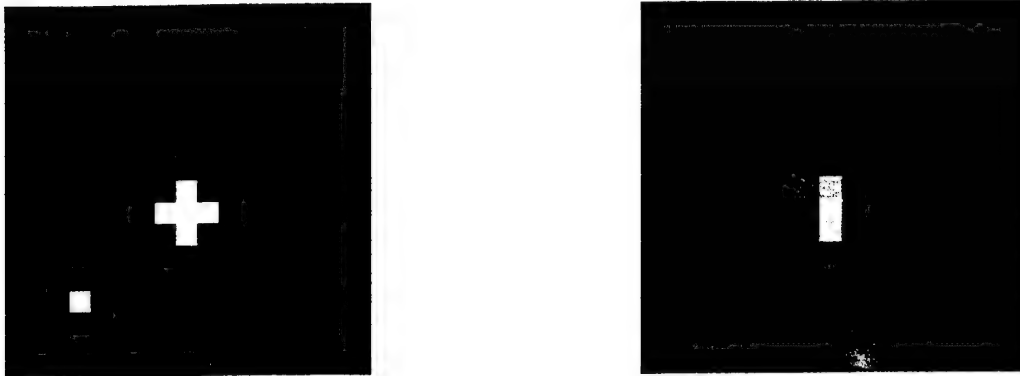


Figure 6. Original object (left) and noisy blurred image (right). The Gaussian PSF was 5 pixels in diameter to 3σ . The system noise floor was 10 input referred photons and the bright pixel signal level was 100 photons per integration period.

The maximum value (bright pixels) in the image was 100 photons per integration period; the minimum value (dark pixels) was zero photons per integration period. The system noise floor was 10 photons per integration period. Convergence properties were studied using a uniform object of 50 photons per integration period as a starting point for the images and plots below.

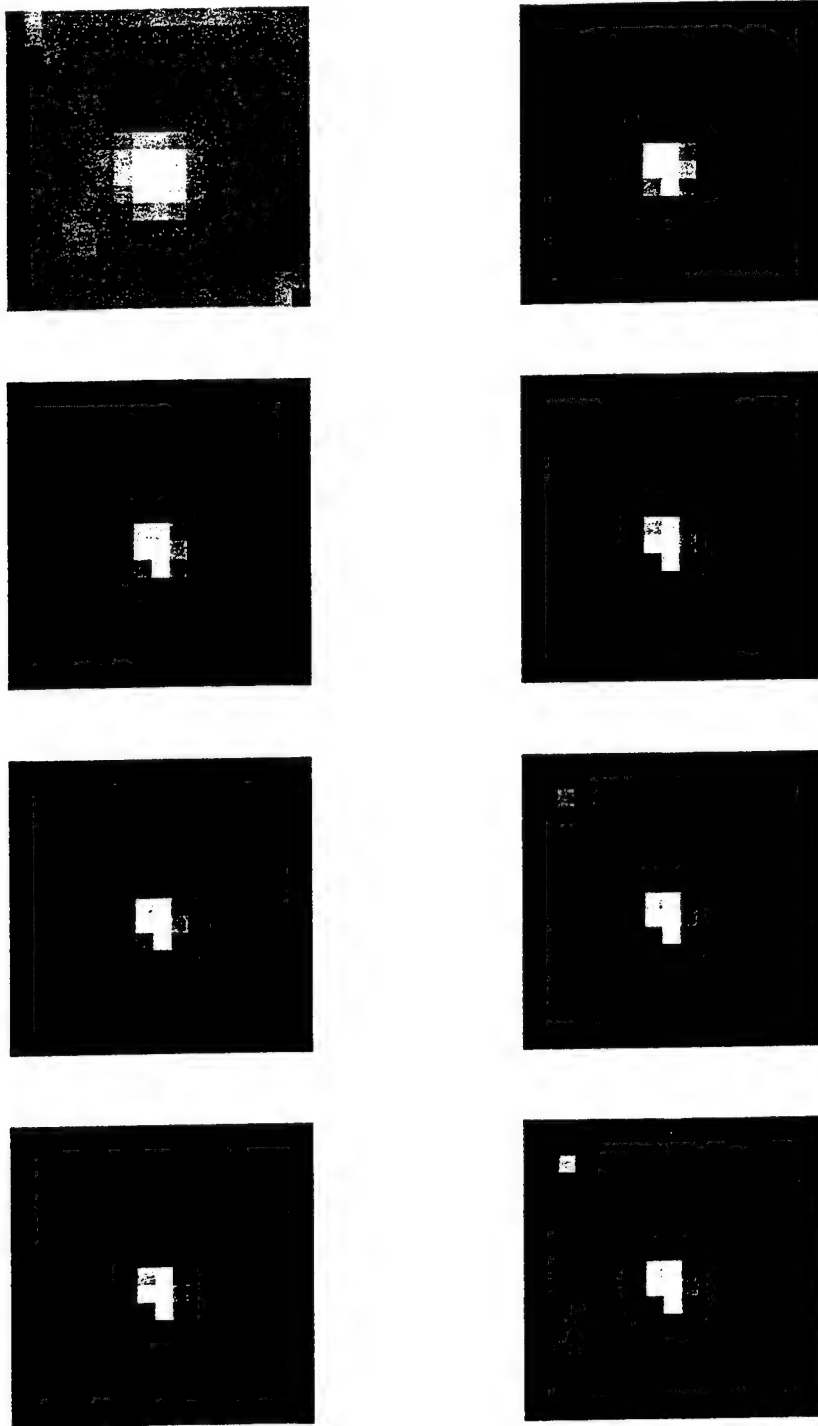


Figure 7. Second, fourth, six and eighth iterations of the new algorithm (left) and MERT (right). The new algorithm deals more effectively with system noise but produces an offset. The black corners are artifacts from a slightly incomplete H matrix.

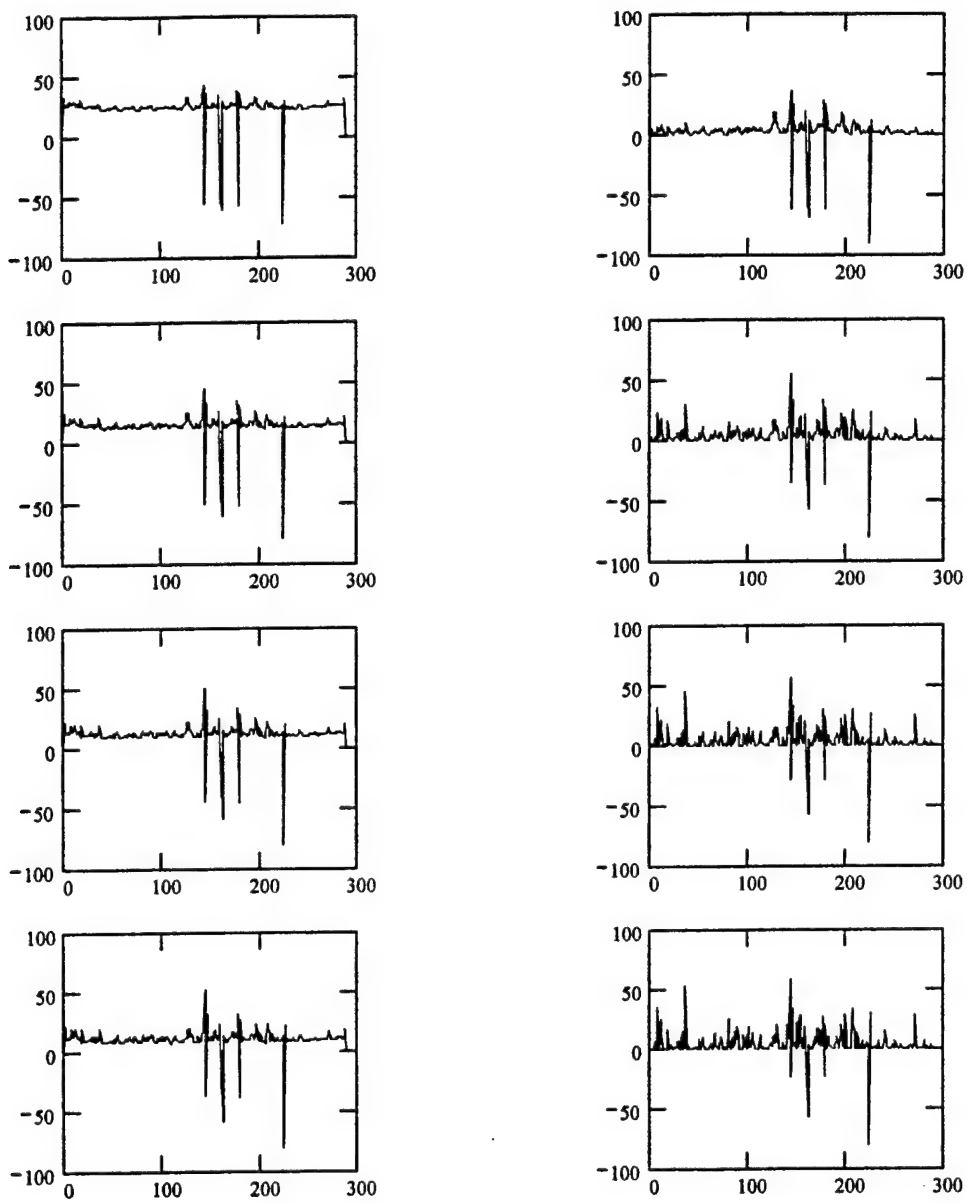


Figure 8. Plots of the error vector $\hat{\mathbf{f}} - \mathbf{f}$ versus the element index (1-289) for the second, fourth, sixth and eighth iterations of the new algorithm (left) and MERT (right). Note in particular the offset pedestal associated with the new algorithm. The starting point for both algorithms was a uniform object of 50 photons per integration period

The convergence properties of the new algorithm can be conveniently studied in a plot of average error versus iteration number. Here we define average error as

$$Error_{ave} = \frac{1}{289} \sum_{j=1}^{289} |\hat{f}_j - f_j| \quad (23)$$

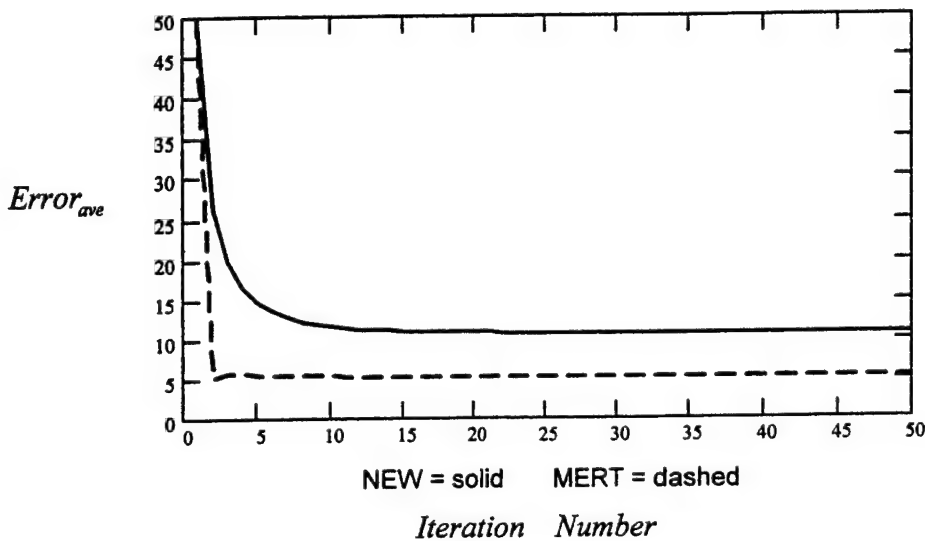


Figure 9. Average error versus iteration number for the new algorithm (solid line) and MERT (dashed line). The primary source of error in the new algorithm is the offset pedestal which is very close to σ_s . The primary source of error in MERT is pixel to pixel reconstruction inaccuracy.

As mentioned in the figure caption above, the primary source of error in the new algorithm is an offset pedestal which is suspiciously close to σ_s . We have inspected plots of the error vector (see Fig. 4) for large iteration numbers and for different combinations of objects and system noise levels and found the same phenomenon. This implies that the new algorithm could be dramatically improved simply by subtracting the value of σ_s from the final image and setting negative pixel values equal to zero. However, it would

be preferable to track down the precise point in the algorithm where the offset is introduced and then fix the problem in a more rigorous fashion.

So far we have described a new image reconstruction algorithm which deals effectively with both photon noise and camera system noise. Good reconstructions have been obtained for an image with a symmetrically blurred point spread function, but this image is not typical of a raw focal plane image from a chromotomographic instrument. In addition, cumbersome mathematical expressions complicate the reconstruction algorithm itself. A final concern is that the algorithm produced an image-wide offset that might have resulted from approximating a ratio of infinite sums by a ratio of definite integrals in the course of the derivation. The following section addresses these three issues.

Algorithm Simplification

The expression for $F1(a,b,c)$ and $F2(a,b,c)$, equations (20) and (21) in our first progress report have been simplified by considering the case of infinite upper limits of the integrals in (18) and (19) from which they were derived. The simplified expressions for $F1$ and $F2$ become

$$F1(a,b,c) = \frac{1}{2} a^{3/2} \sqrt{c} \exp\left[-\frac{b^2 + ac}{2c}\right] \left\{ \frac{2\sqrt{ac(b+c)}}{(a+c)^2} + \frac{(c^2 + a(b^2 + c + 2bc + c^2)) \exp\left[\frac{a(b+c)^2}{2c(a+c)}\right] \sqrt{2\pi} \left[\operatorname{Erf}\left[\frac{\sqrt{a(b+c)}}{\sqrt{2c(a+c)}}\right] + 1 \right]}{(a+c)^{5/2}} \right\}$$

(24)

and

$$F2(a, b, c) = \frac{\sqrt{ac} \exp\left[-\frac{(a-b)^2}{2(a+c)}\right] \sqrt{\frac{\pi}{2}} \operatorname{Erf}\left[\frac{\sqrt{a(b+c)}}{\sqrt{2c(a+c)}}\right] + 1}{\sqrt{a+c}} \quad (25)$$

with $a = (\mathbf{H}\hat{\mathbf{f}}^k)_m$, $b = g_m$, $c = \sigma_s^2$.

The simplified algorithm was tested against the exact algorithm with open-form sums in (15) and the results are shown below in Figure 10.

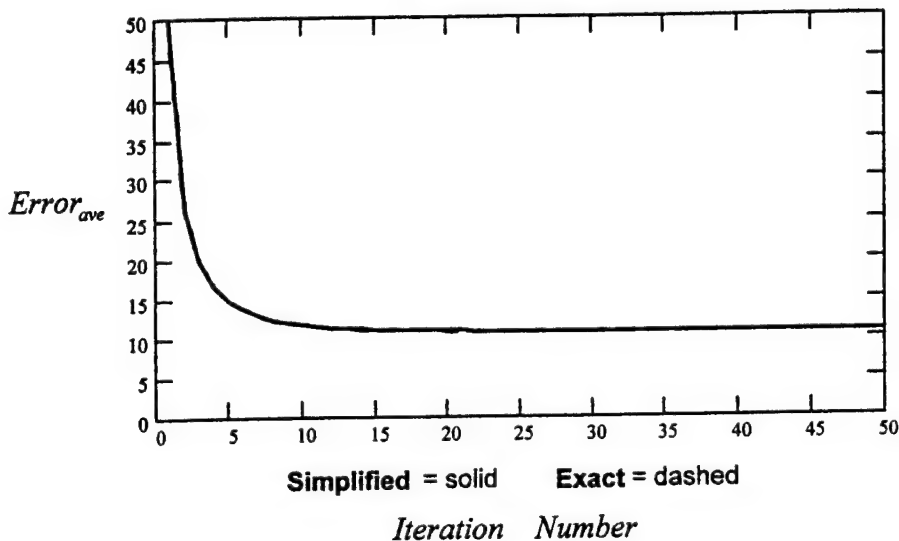


Figure 10. Average Error per pixel, as defined in (23) versus number of iterations. The offset pedestal has not been subtracted here. The same test object and noise conditions as in the Figure 6 was used.

The summations in the open form expression were truncated to a region of plus or minus $5\sigma_s$ about \mathbf{g}_m to avoid excessively long reconstruction times. As can be seen from the figure the ratio-of-integrals approximation is virtually indistinguishable from the exact ratio-of-sums solution.

Image Offset

As mentioned previously, another concern was that the ratio-of-integrals approximation introduced an image-wide offset. Figure 10 addresses this concern as well because it is apparent that both the exact and simplified algorithms converge to the same value, which is just slightly larger than the system noise floor of ten photon arrivals. In Figure 11, the second and eighth iterations of the two algorithms demonstrate that the primary source of error is indeed offset.

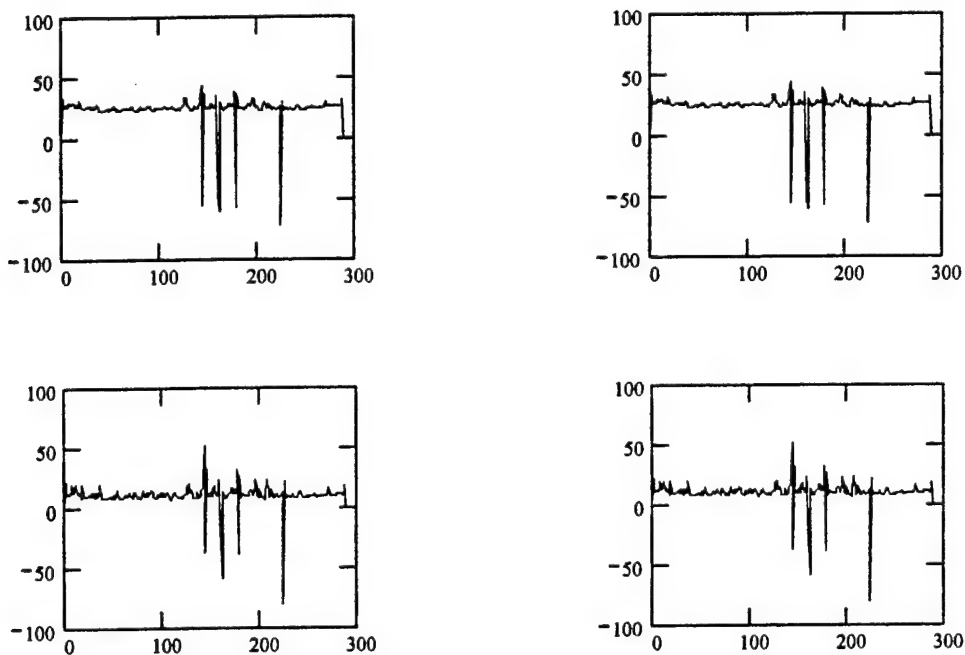


Figure 11. Plots of the error vector, $\hat{\mathbf{f}} - \mathbf{f}$, versus element number for the second (top) and eighth (bottom) iterations of the simplified algorithm (left) and the exact algorithm (right). Pixel to pixel error from noise has been reduced to an offset pedestal.

Accordingly we have concluded that the offset pedestal is inherent in the algorithm and is not a product of the simplifying approximations. Although we cannot prove formally at this point that the algorithm converges to the specified value of the system noise standard deviation, we will subtract it from the final image from here on. The justification is that the pedestal, which is a systematic error, can be subtracted because it is common to all pixels or resolution elements in the reconstruction. Tests have shown that the pedestal is

determined by the value of system noise input to the algorithm regardless of the actual system noise in the input data.

Realistic Simulation

To determine whether the new algorithm is actually useful for chomotomography, an idealized CTIS system was simulated and the algorithm's performance was evaluated against one of our standard reconstruction methods, MART. The simulation mapped a $17 \times 17 \times 10$ (x, y, λ) object cube onto a 111×111 focal plane in four projections plus the center order. For simplicity, the ten spectral slices of the object cube produced exactly ten pixels of lateral dispersion in each projection. Spectrally uniform diffraction efficiency was assumed. Figures 12, 13, 14 show the object cube, the noiseless focal plane image and the focal plane image with temporal Poisson noise and Gaussian system noise with a standard deviation of 12 counts, respectively.

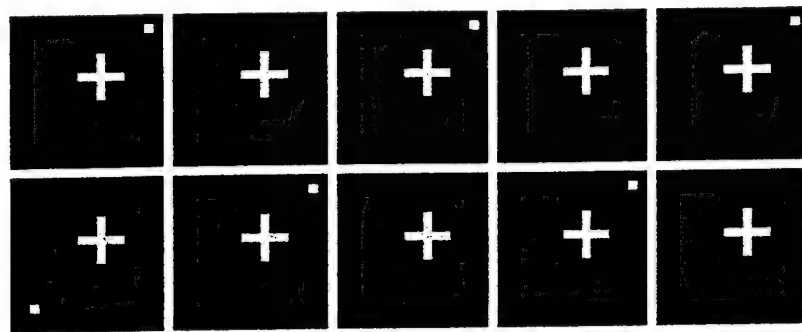


Figure 12. Object cube consisting of ten spectral slices. Wavelength increases left to right, top to bottom. The exact spectral bands are irrelevant because the dispersion is defined in terms of displacement in pixels in the focal plane image.

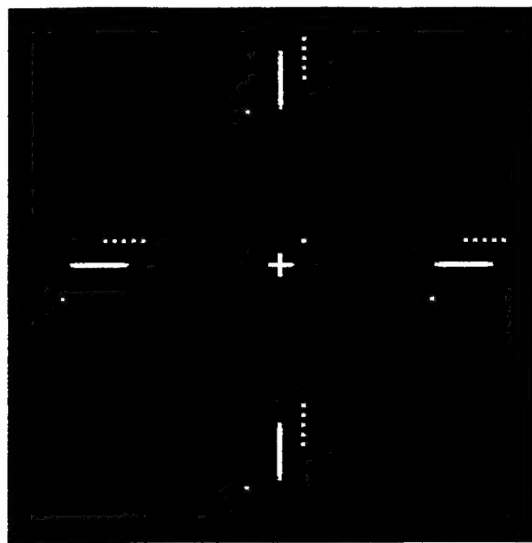


Figure 13. Noiseless focal plane image. Each spectral image of Figure 12 has been displaced radially by one pixel with respect to its short wavelength neighbor.

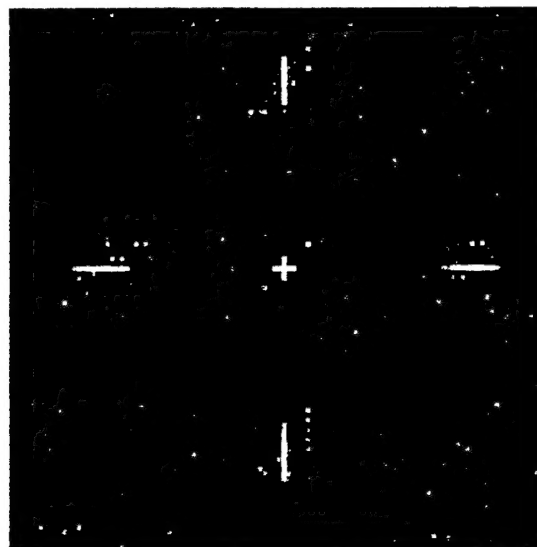


Figure 14. Noisy focal plane image. Poisson noise was introduced to the image of Fig. 4 and added to Gaussian noise with a standard deviation of 12.

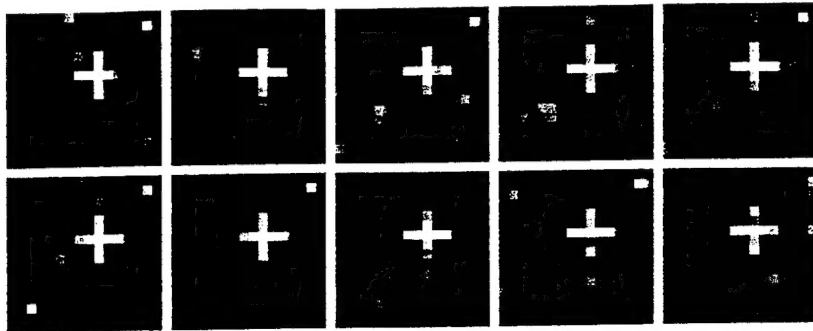


Figure 15. MART reconstruction after eight iterations. Signal-independent noise has propagated through the reconstruction process.

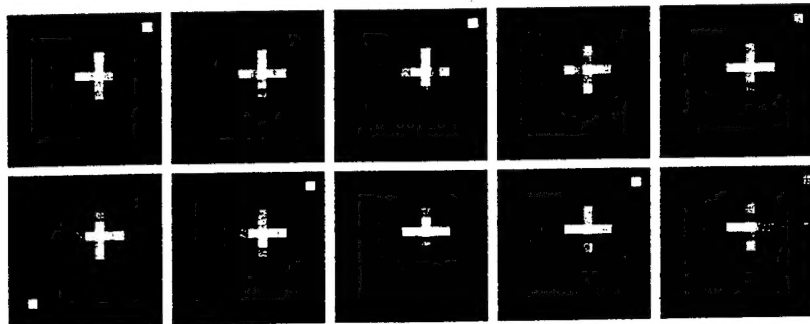


Figure 16. New algorithm reconstruction after eight iterations. Signal-independent noise has been well suppressed in all but the two end bands. It is believed that constant diffraction efficiency versus wavelength in the CTIS simulation caused very low SNR in regions of the projections where spectral overlap is minimal... namely the end bands.

Average error per pixel, was calculated for the two reconstructions, both of which used a uniform initial estimate. MART achieved a value of 5.4 arrivals/pixel whereas the new algorithm achieved a value of 3.3 arrivals/pixel. The reconstruction time for the new algorithm was, surprisingly, only 27 % longer than MART. It should be noted that a similar result could not have been achieved by a 3×3 median window filter applied to either the focal plane image or the final reconstruction since single pixel/resel objects would have been obliterated.

IV. CONCLUSION

Two reconstruction algorithms are described in this report. The first "Principal Component Method", has already proven useful in practice for providing better initial estimates of the object cube to enhance the speed and accuracy of traditional iterative reconstruction methods such as MART and EM. The second, "Extended Maximum Likelihood Method", should prove useful for anticipated low background observations in the MWIR.

V. REFERENCES

1. L.A. Shepp and Y. Vardi, "Maximum likelihood reconstruction for emission tomography", *IEEE Trans. Med. Imaging* MI-1, 113-122 (1982).
2. A. Lent, "A Convergent Algorithm For Maximum Entropy Image Restoration", *Image Analysis and Evaluation*, SPSE Conference Proceedings, Rodney Shaw, ed., pp. 249 – 257 (July 1976).
3. A. Brodzik and J. Mooney, "Singular-value-decomposition projections-onto-convex-sets algorithm for restoration of limited-angle chomotomographic images", *J. Opt. Soc. Am. A*, **16**, No. 2 (Feb 1999).
4. M. R. Descour and E.L. Dereniak, "Computed-tomography imaging spectrometer: experimental calibration and reconstruction results", *Appl. Opt.* **34**, 4817-4826 (1995).
5. J. P. Garcia and E. L. Dereniak, "Mixed-expectation image-reconstruction technique", *Appl. Opt.* **38**, 3745-3748 (1999).
6. B. R. Frieden, *Probability, Statistical Optics, and Data Testing: A Problem Solving Approach* (Springer-Verlag, New York, 1983), p. 51.
7. D. L. Snyder, A.M. Hammoud and R. L. White, "Image recovery from data acquired with a charge-coupled-device camera", *J. Opt. Soc. Am. A* **10**, 1014-1023 (1993).
8. J. Llacer and J. Nunez, "Iterative maximum-likelihood and Bayesian algorithms for image reconstruction in astronomy", in *Restoration of Hubble Space Telescope Images*, R. L. White and R. J. Allen, eds. (Space Telescope Science Institute, Baltimore, Md., 1990), pp. 62-69.